## PAPER

Check for updates

# {Fe$^{2+}$–imidazole} catalyst grafted on magnetic {Fe@Graphitized C} nanoparticles: a robust hybrid–catalyst for H$_2$ production from HCOOH†

Christos Gkatziouras,[a] Christos Dimitriou, [ID][b] Szymon Smykała,[c] Yiannis Deligiannakis [ID] *[b] and Maria Louloudi*[a]

A novel hybrid-catalyst was synthesized *via* covalent grafting of a molecular catalyst {Fe$^{2+}$–Imidazole} on magnetic core–shell {Fe@Graphitized C, Fe@GC} nanoparticles synthesized *via* anoxic flame spray pyrolysis (A-FSP). Transmission electron microscopy (TEM) shows that A-FSP produces a fine C-shell consisting of few graphitized layers, where {Fe$^{2+}$–Imidazole} is covalently grafted. The hybrid catalyst {Fe$^{2+}$–Imidazole}@{Fe@GC} demonstrated highly efficient H$_2$ production from formic acid (HCOOH) at near-ambient conditions of $P = 1$ atm and $T = 80$ °C, yielding >37 Liters of high-purity H$_2$ and a high turnover-number (TON) of >203 000. The {Fe$^{2+}$–Imidazole}@{Fe@GC} catalyst could be easily and efficiently recovered magnetically and reused for at least 12 catalytic cycles, demonstrating significant durability and reusability. Raman, FT-IR, TEM and XRD confirmed the preservation of key structural features of the hybrid catalyst, despite prolonged exposure to reaction conditions. We attribute these beneficial characteristics to the robustness of the FSP-made nanographitized layers and the enhanced efficiency of the {Fe-Imidazole} catalyst when interfaced with nanocarbon.

## 1. Introduction

Hydrogen is a promising clean energy carrier owing to its high energy density (143 MJ kg$^{-1}$) and environmentally benign combustion, producing only water as a byproduct.[1–3] Among various hydrogen storage strategies, liquid organic hydrogen carriers (LOHCs), such as formic acid (HCOOH, FA), have gained significant attention owing to their efficient hydrogen release, low decomposition temperature, and minimal CO formation. These attributes make FA a viable candidate for practical hydrogen storage and utilization.[4–8]

Thus far, the catalytic dehydrogenation of FA has been extensively studied, leading to the development of efficient homogeneous and heterogeneous molecular catalysts. Specifically, these include noble metal catalysts, *e.g.* iridium (Ir),[9] platinum (Pt),[10] and ruthenium (Ru),[11] which demonstrated high efficiency in the presence of suitable organic ligands; thus, currently, there is convergent evidence that ligands incorporating nitrogen (N) or phosphorus (P) play a crucial role in

stabilizing active sites and modulating electron density, thereby enhancing catalytic activity and longevity.[12–15] However, the high cost, limited availability, and environmental concerns associated with noble metals have prompted efforts to explore non-noble metal alternatives, such as iron (Fe),[16] cobalt (Co),[17] and nickel (Ni).[18] In this context, our laboratory has made significant advancements by designing highly efficient Fe-based catalytic systems, *e.g.* including a [FePP$_3$Lγ]/H$_2$N@SiO$_2$ catalyst, which achieved a TON of 29 372 and a reaction rate of >100 mL min$^{-1}$.[19]

With the aim of achieving industrial application, heterogeneous molecular catalysis has emerged as a viable alternative to homogeneous catalysis as it offers improved catalyst stability, reusability, and ease of separation from reaction mixtures. This approach involves immobilizing homogeneous catalysts onto solid supports such as silica (SiO$_2$),[20] carbon matrices[21,22] (*e.g.* activated carbon and carbon nanotubes), and metal–organic frameworks (MOFs).[23] These materials provide high chemical stability, large surface areas, and uniform metal dispersion, which can contribute to enhanced catalytic performance and durability.[24,25] In this context, we have demonstrated various promising options for Fe catalysts grafted on SiO$_2$.[19,26] Recently, by immobilizing imidazole onto silica *via* Si–O–Si bonds, we developed a novel catalyst [Fe(II)/imidazole/PP$_3$], which exhibited a high TON of ~23 000 and a TOF of >5500 h$^{-1}$. However, as we have shown through careful analysis, prolonged acidic exposure, as required for reusability, degraded the stability of this catalyst *via* the C–O–C bond cleavage of the silane-spacer,

*[a]Laboratory of Biomimetic Catalysis and Hybrid Materials, Department of Chemistry, University of Ioannina, GR45110 Ioannina, Greece. E-mail: mlouloud@uoi.gr*

*[b]Laboratory of Physical Chemistry of Materials & Environment, Department of Physics, University of Ioannina (UOI), Ioannina, 45110, Greece. E-mail: ideligia@uoi.gr*

*[c]Institute of Engineering Materials and Biomaterials, Silesian University of Technology, 18a Konarskiego St, Gliwice 44-100, Poland*

† Electronic supplementary information (ESI) available. See DOI: https://doi.org/10.1039/d5ta03079j

This journal is © The Royal Society of Chemistry 2025

*J. Mater. Chem. A*, 2025, **13**, 21659–21671 | 21659

reducing the catalyst reusability.[26] Subsequently, we have explored the option of replacing the $SiO_2$ matrix with a carbon matrix towards the aimed durability. Carbon materials are highly advantageous for catalytic applications due to their large surface area, porosity, chemical and thermal stability, as well as their versatility in surface functionalization, which allows for the tailoring of their properties to optimize catalytic performance.[27,28] Surface functionalization enables the introduction of active groups that strengthen the interaction between catalytic metal centers and the carbon support, thereby facilitating putative synergistic effects that can enhance overall catalytic performance.[29–31] For instance, electron transfer between carbon and the metal catalyst can improve both stability and catalytic efficiency.[32] The mechanical strength of carbon-based materials also plays a crucial role in maintaining the structural integrity of catalysts, allowing them to endure operational stresses and regeneration processes. This durability is vital for ensuring catalyst recyclability, enabling repeated use across multiple cycles without substantial loss in performance.[30,33,34]
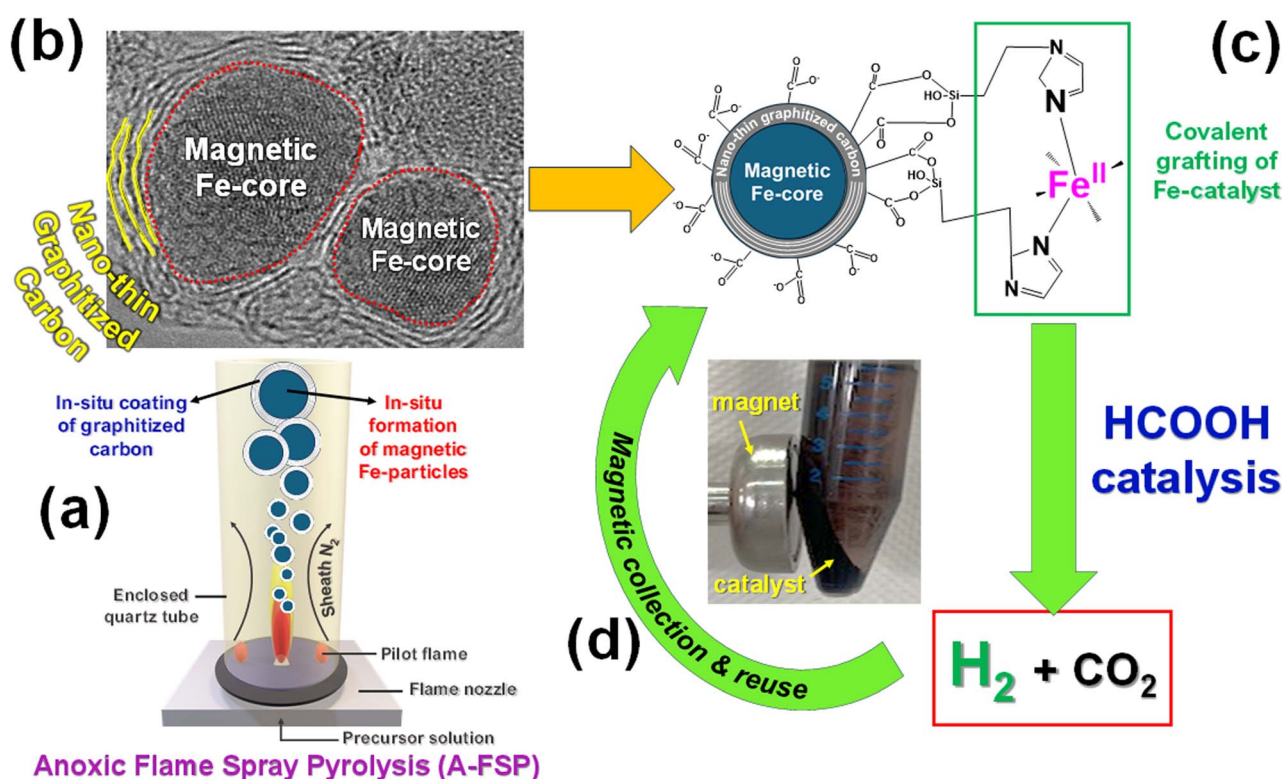
Numerous studies have explored metal nanoparticles supported on carbon matrices, with Pd/C catalysts gaining significant attention due to their high catalytic activity, ease of synthesis, and recyclability.[22,35–39] However, challenges, such as metal nanoparticle agglomeration, which leads to reduced active surface area and adsorption of toxic byproducts, limit

their long-term efficiency.[40] Additionally, the high cost of palladium necessitates the development of more cost-effective and sustainable alternatives.[41]

To overcome these challenges, we have developed[43] a cost-effective {$Fe^{2+}$–imidazole} catalyst, which, when immobilised on activated carbon, exemplifies a highly efficient hybrid catalyst achieving a remarkable TON >353 000 over 8 cycles.[42] Herein, we further advanced this technology by grafting the {$Fe^{2+}$–imidazole} catalyst onto nanographitized carbon tightly associated with the magnetic Fe-core, hereafter codenamed {Fe@Graphitized C, Fe@GC}. Thus, we have produced a novel nanohybrid {$Fe^{2+}$–imidazole}@{Fe@GC}; see Fig. 1. This approach aimed to achieve a triple gain: [i] high $H_2$ production, [ii] enhanced reusability and [iii] easy recovery *via* magnetic collection.

Previous works have shown encouraging results, indicating that the chemical stability of graphitized carbon can enhance durability and reusability, making it highly promising for catalysis, environmental remediation, and energy conversion.[43–46] Herein, the synthesis of {Fe@Graphitized C} particles was performed using an anoxic flame spray pyrolysis (A-FSP) process.[47–51]

This enabled the production of high-quality {Fe@Graphitized C, Fe@GC} particles, in which a nano-thin coating of a few graphitized layers hermetically encapsulates the Fe core; see



**Fig. 1** The synthesis pathway of the {$Fe^{2+}$–imidazole}@{Fe@GC} hybrid: (a) the {Fe@GC} synthesized *in situ via* anoxic flame spray pyrolysis (A-FSP); (b) TEM images show the formation of fine-coating of few-graphitized layers around the magnetic Fe-core; (c) {Fe@GC} functionalized by covalent grafting of [$Fe^{2+}$–imidazole] complexes *via* sol–gel chemistry; (d) the catalytic {$Fe^{2+}$–imidazole}@{Fe@GC} material was evaluated in formic acid dehydrogenation (FADH) for 12 repetitive sequential cycles; after each cycle, the catalyst was directly and easily recovered by a magnet due to its magnetic Fe-core.

Fig. 1. Then, we covalently grafted a {$Fe^{2+}$–imidazole} catalyst onto {Fe@GC} to produce stable {$Fe^{2+}$–imidazole}@{Fe@GC} hybrids.

Specific aims of the present work include: [i] to develop hybrid {$Fe^{2+}$–imidazole}@{Fe@GC} materials using A-FSP and grafting technologies, [ii] to validate and optimize their efficiency for $H_2$ production *via* HCOOH dehydrogenation at near ambient conditions, [iii] to study their recovery/reusability in multiple cycles of $H_2$ production and [iv] to understand the key-role of the graphitized-nanocarbon on the performance and stability of the hybrid {$Fe^{2+}$–imidazole}@{Fe@GC}.

## 2. Experimental methods

### 2.1 Instrumentation

**2.1.1 Powder X-ray diffraction.** Powder X-ray diffraction (pXRD) analysis was conducted at ambient temperature utilizing a Bruker D8 Advance diffractometer. The instrument was equipped with Cu Kα radiation ($\lambda = 1.5406$ Å) and a secondary monochromator, operating at 36 kV and 36 mA. Data were acquired over a $2\theta$ range of 10° to 80°.

**2.1.2 $N_2$ porosimetry.** The $N_2$ adsorption–desorption isotherms were measured at 77 K on a NOVAtouch LX2 Quantachrome porosimeter. Prior to the measurements, the samples were degassed at 80 °C for 16 h under a vacuum. The specific surface area (SSA) was determined using the Brunauer–Emmett–Teller (BET) method for adsorption and desorption data points. The specific surface area was found using adsorption data points in the relative pressure $P/P_0$ range of 0.1–0.3. While the density functional theory (DFT) method was used to determine the pore radius using absorption data points from 0.35 to 0.99 $P/P_0$, the total pore volume was obtained at the 0.99 $P/P_0$ points.

**2.1.3 Raman spectroscopy.** Raman spectra were collected using a HORIBA XploRA PLUS Raman microscope integrated with an Olympus BX41 optical microscope. Prior to measurements, each powdered sample was pressed into a pellet by gently compressing it between two glass plates. A 1 mW laser power was used, which was experimentally optimized to ensure that the crystal phase remained unaffected during the analysis. A 785 nm diode laser served as the excitation source, with the beam focused through the microscope. Spectral acquisition was performed under the following conditions: an exposure time of 10 seconds per scan, with 30 accumulations.

**2.1.4 Thermogravimetric analysis (TG-TDA).** The organic content in our catalytic materials was determined through thermogravimetric analysis (TGA) using a SHIMADZU DTG-60 instrument coupled with a TA-60 WS analyzer. Approximately 30 mg of the sample was placed in a platinum crucible positioned on one arm of the thermobalance, while an empty platinum crucible served as a reference on the opposite arm. The analysis was conducted within a temperature range of 20 to 700 °C, with a heating rate of 10 °C $min^{-1}$, under a synthetic air atmosphere.

**2.1.5 Transmission electron microscopy (TEM).** The morphology, nanostructure, and chemical composition of the nanoparticles were examined using an FEI Titan 80–300 STEM microscope at a 300 kV accelerating voltage. STEM images were obtained with a beam convergence semiangle of 21.5 mrad.

**2.1.6 Scanning electron microscopy (SEM).** Images were obtained using a Thermo Fisher Pharos Phenom G2 field-emission scanning electron microscope (FE-SEM) (Waltham, MA, USA) operating under high-vacuum conditions (0.1 Pa) with an accelerating voltage of 15 kV. Both backscattered and secondary electron detectors were utilized at a 20 : 80 ratio. Prior to imaging, the samples were coated with a 5 nm layer of chromium using a Quantum Design Q150T Plus sputter coater (Darmstadt, Germany). Additionally, energy-dispersive spectroscopy (EDS) analysis was performed using the same instrument to investigate the surface chemical composition of the nanocatalysts.

**2.1.7 Solution potential.** The solution potential ($E_h$) was continuously monitored *in situ* throughout the experiment using a combined platinum (Pt) ring electrode (Metrohm 6.0451.100). This electrode was directly integrated into the reactor system to ensure real-time measurement of the reaction potential within the solution.

**2.1.8 Fourier-transform infrared spectroscopy (FTIR).** FTIR spectra were recorded using a Nicolet IS5 system equipped with OMNIC FTIR Software version 9.2.86. The spectra were collected over the range of 4000 to 400 $cm^{-1}$, with a resolution of 2 $cm^{-1}$ and an average of 100 scans.

### 2.2 Synthesis of core–shell {Fe@Graphitized C, Fe@GC} by anoxic flame spray pyrolysis (A-FSP)

The {Fe@GC} particles were synthesized using our FSP set-up described earlier[50,52] with a modification to create an oxygen-lean atmosphere. Specifically, the flame was hermetically enclosed with a quartz tube to prevent ambient air entrainment; see Fig. 1. In addition, an $N_2$ sheath was used to control the anoxicity of the combustion atmosphere.

The Fe precursor solution was prepared by dissolving 0.4 M iron naphthenate (Alfa Aesar, 38% in mineral spirits, 6% Fe) in xylene (Sigma-Aldrich, purity >97%). Based on systematic screening, the optimal A-FSP conditions employed were as follows: the flame was enclosed using a 40 cm quartz tube, with no gap between the tube and the burner. The solution was fed through a capillary at 2 mL $L^{-1}$ and dispersed by 2 L $min^{-1}$ $O_2$ (Linde, purity >99%), respectively, into a stoichiometric, self-sustaining oxygen–methane (2.5 L $min^{-1}$, 1.5 L $min^{-1}$) pilot flame to initiate combustion. The pressure drop at the nozzle tip was set at 2 bar, and an additional 20 L $min^{-1}$ sheath $N_2$ was used. The product powder was collected using a vacuum pump (Busch V40) on a glass microfiber filter (Albet Labscience GF6 257 mm in diameter). The burner-to-filter distance (BFD) was fixed at 69 cm. The nanomaterials were collected and stored in glass vials under an inert argon atmosphere until use. This material is listed as Fe@C-prist in Table 1.

**2.2.1 Post-FSP treatment.** Post-FSP treatment of {Fe@GC} nanoparticles was conducted to investigate and optimize the phase composition, particle size, and carbon graphitization. A calcination protocol was performed at $T = 600$ °C for 24 h under a reducing Varigon H5 gas (95% Ar + 5% $H_2$) to enhance the

This journal is © The Royal Society of Chemistry 2025

*J. Mater. Chem. A*, 2025, **13**, 21659–21671 | **21661**

**Table 1** Structural and surface characteristics of pristine, post-calcined and post-functionalized {Fe$^{2+}$–imidazole}@{Fe@GC} hybrid

| Material | Material configuration | Phase composition (%) ($\pm 1$)/crystallite size (nm) ($\pm 0.5$) | | | | | $d_{BET}$ (nm) | SSA (m$^2$ g$^{-1}$) ($\pm 1$) | Pore volume (cm$^3$ g$^{-1}$) ($\pm 0.005$) |
|---|---|---|---|---|---|---|---|---|---|
| | | Magnetite Fe$_3$O$_4$ | Wustite FeO | Martensite C$_{0.2}$Fe$_{1.8}$ | Iron Fe$^0$ | Cementite Fe$_3$C | | | |
| Fe@C-prist | FSP-made core@shell Fe@carbon (pristine) | 24/24 | 29/28 | 22/9 | — | 25/26 | 12 | 83 | 0.199 |
| Fe@C-calc | Fe@C-prist calcined at 600 °C for 24 h under Varigon H5 | 32/15 | 5/10 | 3/8 | 53/38 | 7/17 | 6 | 157 | 0.379 |
| Fe@C-graf | Fe@C-calc grafted with Fe$^{2+}$–imidazole *via* silane | 29/14 | 4/23 | 6/8 | 49/55 | 12/20 | 7 | 101 | 0.358 |
| Fe@C-aftercat | Fe@C-graf after 12 cycles of FADH catalysis | 27/25 | 4/22 | 4/7 | 41/53 | 24/24 | 10 | 84 | 0.218 |

graphitization of carbon by facilitating the removal of oxygen-containing functional groups, thereby promoting a higher degree of structural ordering. Additionally, the reducing conditions influenced the phase evolution of iron, stabilizing metallic Fe or promoting the formation of FeC phases as verified by XRD results; see Fig. 2a. The so-obtained material is codenamed Fe@C-calc, as listed in Table 1.

### 2.3 Synthesis of the {Fe$^{2+}$–imidazole}@{Fe@GC} hybrid
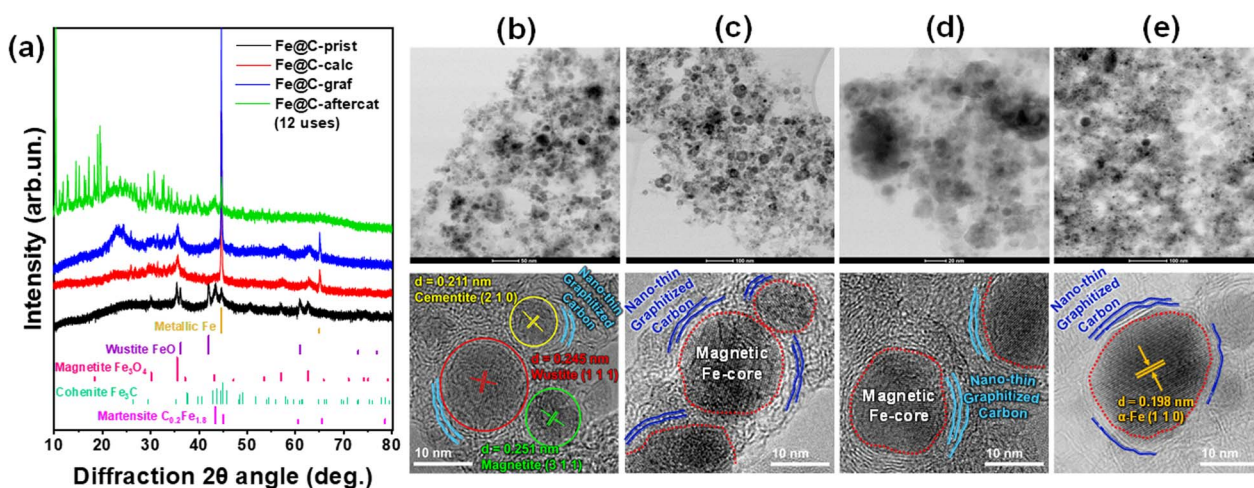
For the synthesis of {Fe$^{2+}$–imidazole}@{Fe@GC}, 1 mmol of 3-chloropropyltrimethoxysilane was added to 10 mL of methanol (MeOH) containing 1.2 mmol of imidazole. The resulting mixture was stirred at 80 °C for 24 h. Subsequently, the reaction mixture was cooled to 40 °C, followed by the addition of 0.5 mmol of [Fe(BF$_4$)$_2$·6H$_2$O] (Sigma Aldrich) dissolved in 10 mL of MeOH, and stirring was continued for an additional 2 h. Thereafter, 0.4 g of FSP-made {Fe@C-calc} matrix was introduced into the reaction medium along with 5 mL of ethanol (EtOH), and the system was stirred at 60 °C for 24 h. The solid product was then collected, washed twice with 5 mL of MeOH and 5 mL of EtOH, and dried under vacuum at 70 °C using

a drying pistol. The obtained hybrid material is depicted in Fig. 1 and is named as Fe@C-graf in Table 1.

### 2.4 Catalytic H$_2$ production process

The catalytic reactions were conducted in a double-walled reactor under an Ar atmosphere with continuous stirring, maintaining a stable temperature of 80 $\pm$ 1 °C using a heated magnetic stirrer. The reactor was directly connected to a gas chromatography (GC) system (Shimadzu GC-2014 Gas Chromatograph equipped with a thermal conductivity detector (GC-TCD) and a Carboxen-1000 column) for real-time gas analysis and identification. The total gas volume was determined using a manual gas burette.

In the catalytic reaction, 15 μmol of {Fe$^{2+}$–imidazole}@{Fe@GC} was introduced into a 7 mL reaction mixture composed of 5 mL propylene carbonate (PC) [Merck] and 2 mL formic acid (FA) {Sigma-Aldrich, [97.5/2.5H$_2$O] (v/v)}. Following an incubation period of 30 minutes under continuous stirring, 7.5 μmol of PP$_3$ {tris[2-(diphenylphosphino)ethyl]phosphine, Sigma-Aldrich, purity of 98%}, was added to initiate gas evolution. The catalytic performance was evaluated using TONs and



**Fig. 2** (a) XRD patterns of all the studied materials along with the JCPDS cards of the dominant phases. (b–e) STEM (top) and HRTEM (bottom) images of (b) Fe@C-prist, (c) Fe@C-calc, (d) Fe@C-graf and (e) Fe@C-aftercat (12 uses).

TOFs equations.[19,26,42,53] The continuous feeding process was sustained by the incremental addition of 2 mL of FA each time, and 1800 mL of gas ($H_2 + CO_2$) was produced until the reaction was completed.

# 3. Results

## 3.1 Characterization of materials

XRD analysis (Fig. 2a and S2 in ESI,†) shows that the dominant diffraction peaks of Fe@C-prist correspond to magnetite ($Fe_3O_4$) [JCPDS 19-0629], wüstite (FeO) [JCPDS 06-0615], martensite ($C_{0.2}Fe_{1.8}$) [JCPDS 44-1289] and cohenite ($Fe_3C$) [JCPDS 35-0772], confirming the presence of a core–shell structure. We have calculated the composition of each phase, and the crystallite sizes of these dominant phases are listed in Table 1. Additionally, a broad peak at $2\theta = 26°$ was attributed to the graphitic carbon.[46] Upon calcination at 600 °C under $H_2$/Ar (5/95), a partial reduction of $Fe_3O_4$ and FeO occurred, leading to the formation of metallic iron ($Fe^0$) [JCPDS 06-0696]. Simultaneously, an oxidation process resulted in the emergence of traces of luogufengite ($\varepsilon$-$Fe_2O_3$) [JCPDS 16-0653], while $Fe_3O_4$ and $Fe_3C$ were retained, and additional carbide phases, such as $Fe_7C_3$ [JCPDS 89-2005], were detected, as shown in Fig. S2.† After grafting, the XRD profile of Fe@C-graf was unchanged (Fig. 2a), indicating that the Fe-phases were not affected by the grafting process. This was verified by HR-TEM, as shown in Fig. 2b and c, which show the Fe-core and graphitized-C coatings in the grafted Fe@C-graf, corresponding to the {$Fe^{2+}$-imidazole}@{Fe@GC} hybrid.

Further analysis by SEM-EDX spectra, see Fig. S5 in ESI,† confirms the non-altered elemental arrangement in the Fe@C-calc and Fe@C-graf materials. TEM analysis provides critical insights into the structural and morphological evolution of the catalytic material under different stages of catalytic use/reuse. Specifically, Fig. 2b illustrates the TEM image of the pristine material (Fe@C-prist), showing the Fe core and its coating with nano-thin graphitized carbon. The TEM image reveals a well-formed graphitized shell that hermetically coats the Fe particle, forming a uniform and well-defined structure.

The presence of distinct lattice fringes confirms the crystallinity of the Fe core. Miller planes of three different $d$-spacings are resolved with $d = 0.211$ nm representing the cementite (2 1 0) lattice,[54] $d = 0.245$ nm representing the wustite (1 1 1) phase[55] and $d = 0.251$ nm representing the magnetite (3 1 1) phase.[56] Fig. 2c and d show the TEM images of Fe@C-calc and Fe@C-graf, respectively, demonstrating that after calcination and grafting, the magnetic Fe core encapsulated by nano-thin graphitized carbon remained intact.

EDS/EDX spectra obtained from TEM/STEM analysis in Fig. S6a† of the pristine sample display multiple iron peaks, indicating the dominance of Fe within the material. Additionally, the presence of oxygen suggests the formation of iron oxides, while the detection of carbon corroborates the presence of the protective carbon shell. Upon calcination, no significant morphological changes are observed (Fig. 2b); however, the iron core appears denser and exhibits enhanced crystallinity due to the removal of amorphous carbon during the process, while the

integrity of the graphitized carbon shell remains preserved. For the functionalized sample (Fig. 2d), the core–shell structure is retained, yet an increased heterogeneity in contrast is observed. This variation suggests successful surface functionalization, potentially altering the electron density at the carbon interface. Additionally, STEM reveals partial nanoparticle agglomeration, though the core–shell structure remains unaffected. The EDS/EDX spectrum for Fe@C-calc (Fig. S6b in ESI†) is similar to those of Fe@C-prist, showing only peaks corresponding to C, Fe, and O, while the spectrum of Fe@C-graf (Fig. S6c†) exhibits additional peaks due to the presence of N and Si as result of imidazole grafting *via* Si–O-anchoring sites. These findings highlight the successful FSP contribution and the subsequent successful grafting process for the synthesis of {Fe@Carbon@Imidazole-$Fe^{2+}$}, which preserves its structural robustness while maintaining its core–shell architecture, a key aspect of its potential catalytic applications.

For further investigation of the surface characteristics of the materials and the structural modifications occurring during synthesis, Raman and FT-IR spectroscopy were employed. Fig. 3 depicts the Raman spectra of our materials, exhibiting two characteristic peaks at 1313 $cm^{-1}$ and 1598 $cm^{-1}$. Specifically, the peak at 1598 $cm^{-1}$ corresponds to the graphitic G-band, which is indicative of $sp^2$-hybridized carbon structures and represents the fundamental feature of graphite. On the other hand, the peak at 1313 $cm^{-1}$ is attributed to lattice defects, structural disorder, and low-symmetry configurations within the graphite framework.[57–59] These characteristic bands indicate the presence of $sp^2$ and $sp^3$ carbons within the matrices in alignment with the observation of the $I_D/I_G$ ratio, which serves as a key tool for detecting structural alterations in carbon-based materials.

Furthermore, the peak observed at 593 $cm^{-1}$ in Fig. S4† is associated with wüstite (FeO). Additional peaks correspond to
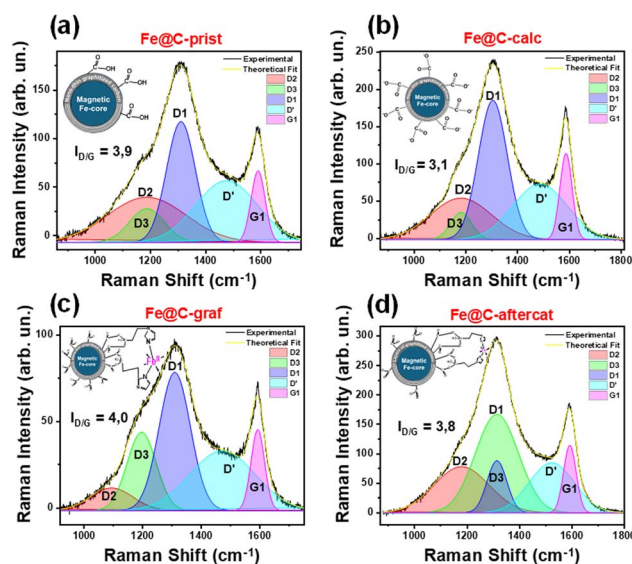


Fig. 3 Raman spectra of (a) Fe@C-prist, (b) Fe@C-calc, (c) Fe@C-graf, and (d) Fe@C-aftercat (12 uses). The colored peaks correspond to the deconvolution of D and G subcomponents.

This journal is © The Royal Society of Chemistry 2025

*J. Mater. Chem. A*, 2025, **13**, 21659–21671 | **21663**

the oxidation products of wüstite, specifically hematite, at approximately 200 cm$^{-1}$ and 300 cm$^{-1}$ and magnetite at 682 cm$^{-1}$.[60,61]

To focus on the two main distinct Raman peaks, *i.e.* G and D, which correspond to distinct vibration modes in carbon-based materials, their deconvolution using Gaussian fitting was performed (Fig. 3). The G band corresponds to the $E_{2g}$ vibration of sp$^2$-bonded carbon pairs, while the D band is linked to the $A_{1g}$ mode, akin to an in-plane breathing vibration. D1 peak (1350 cm$^{-1}$) is associated with the presence of sp$^3$ hybridized carbon atoms and edge defects. D2 (1200 cm$^{-1}$), D3 (1500 cm$^{-1}$) and D' (1620 cm$^{-1}$) are additional defects related to peaks that are signs of amorphous carbon contribution and sp$^2$-sp$^3$ hybridization transitions or secondary disorder effects. G1 (1580 cm$^{-1}$) indicates the graphite like carbon structure, representing the in-plane vibration mode of graphitic domains.[62,63]

As observed, in the three treatments of our sample (FSP-pristine, calcined, and grafted), the $I_D/I_G$ ratios indicate a significant degree of structural disorder in the carbon matrix. This disorder arises from the flame spray pyrolysis process, where rapid cooling and combustion conditions influence the material's morphology,[50] as analysed recently for our FSP-made carbon-coated TiO$_2$.[64] Here, the $I_D/I_G$ ratios further confirm the presence of both sp$^2$-and sp$^3$-hybridized carbon domains. Notice that the nano-thin graphitic carbon clearly resolved by TEM images (Fig. 2b–e), corresponds to the non-negligible D-band in Raman (Fig. 3), which originates from the local non-planar geometry of the graphitic carbon layers that bend to encapsulate the spherical magnetic Fe-particles. In addition, strains in the sp$^2$ carbon lattice and structural defects may break the perfect sp$^2$-symmetry of graphite, rendering the -otherwise forbidden- D band, Raman-active.[65]

Upon calcination at 600 °C under an Ar/H$_2$ atmosphere, the $I_D/I_G$ ratio decreases to 3.1, indicating a partial reduction of amorphous carbon and increased sp$^2$-graphitization. Following the immobilization of [Fe$^{2+}$–imidazole] functionalities, the $I_D/I_G$ ratio increased to 4.0, indicating that grafting introduces additional distortion and structural defects within the carbon framework. Overall, the present Raman data, together with TEM, confirm that the FSP-made Fe@GC particles retain their key structural features during calcination and optimization (Fe@C-calc) and grafting process (Fe@C-graf).

The FT-IR spectra depicted in Fig. 5a confirm the successful grafting in Fe@C-graf. Specifically, the FTIR spectrum exhibited a broad absorption band at 3426 cm$^{-1}$, attributed to O–H and N–H stretching vibrations.[66] Additionally, distinct peaks were identified at 3043 cm$^{-1}$ and 2933 cm$^{-1}$, corresponding to aliphatic C–H stretching vibrations.[67] The absorption band at 1633 cm$^{-1}$ was assigned to aromatic C=C stretching vibrations, while the peak at 1062 cm$^{-1}$ indicated the presence of C–O bonds. Finally, the characteristic Fe–O vibrations were observed at 580 cm$^{-1}$.

The textural properties of the core–shell nanoparticles were also evaluated using N$_2$ adsorption–desorption isotherms. Note that FSP-made nanoparticles generally do not have pores; hence, the vacuum space between nanoparticles is considered to be the theoretical porosity. As shown in the BET analysis (Fig. S3 in ESI†), the pristine material exhibited a specific surface area (SSA) of 83 m$^2$ g$^{-1}$, indicative of type IV isotherms.[68] Following calcination, the SSA increased to 157 m$^2$ g$^{-1}$, suggesting enhanced porosity due to the partial removal of amorphous carbon and structural reorganization, as corroborated by Raman spectroscopy (Fig. 3b). Further functionalization of the surface with [Fe$^{2+}$–imidazole] resulted in a decrease in SSA to 101 m$^2$ g$^{-1}$, accompanied by a decrease in pore volume. Analysing the pore size and volume trends (Fig. 5c) reveals that post-calcination of Fe@C- calc leads to an increase in pore volume. Specifically, Fe@C-prist exhibits a total pore volume of 0.199 cm$^3$ g$^{-1}$, which nearly doubles to 0.379 cm$^3$ g$^{-1}$ after calcination. This change is attributed to the effects of calcination under reducing conditions (5% H$_2$/Ar), which enhance the graphitization of the carbon layers. Fig. 5c also shows pore sizes ranging from 4 nm to 60 nm, which could potentially enhance catalytic kinetics. After grafting, the pore volume remains stable at 0.358 cm$^3$ g$^{-1}$, indicating structural integrity.

## 3.2 Catalytic H$_2$ production from HCOOH

The {Fe$^{2+}$–imidazole}@{Fe@GC} hybrid was evaluated as a catalyst in formic acid dehydrogenation (FADH) in the presence of PP$_3$ in propylene carbonate. Fig. 4a shows that the catalyst was able to catalyze 8 mL of FA through continuous feeding, providing 6.4 L of gas with a reaction rate of 43 mL min$^{-1}$, TONs of 17 447 and TOFs of 4985 h$^{-1}$ (Table 2). According to the well-known reaction path,[69] the evolved gas consisted exclusively of H$_2$ : CO$_2$ {50% : 50%} (Fig. S8†). Herein, this was confirmed by online gas chromatography with a thermal conductivity detector (GC-TCD) and the analysis confirmed that it consisted exclusively of H$_2$ and CO$_2$ in a 1 : 1 ratio (Fig. S8†). The complete absence of CO, demonstrates the high selectivity of the Fe-imid catalyst.[69] For completeness, a control experiment using a simple mixture of the particles and the Fe ions [Fe@C/Fe$^{2+}$/PP$_3$] yielded only 120 mL of gas (Fig. 4a), thus demonstrating that the covalent-grafting of the {Fe-imidazole} complex on the {Fe@GC} surface is of key-importance for the H$_2$-FADH by the {Fe$^{2+}$–imidazole}@{Fe@GC} hybrid. All catalytic experiments were conducted in triplicate, yielding consistent outcomes within ±5% (not shown).

To further understand the physicochemical catalytic events, we monitored the solution potential ($E_h$). As shown,[26,42,70-74] monitoring of $E_h$ in FADH catalysis provides information on the evolution of the key-reducing components of the system, *i.e.*, a negative $E_h$ should be established beyond a threshold-value for successful H$_2$ production *via* FADH.[70] In this context, the $E_h$ data in Fig. 4c demonstrate that the hybrid catalyst {Fe$^{2+}$–imidazole/PP$_3$}@{Fe@GC} creates the necessary reducing $E_h$ profile, suitable for fast FADH catalysis *via* the generation of key-determinant hydride species.[70]

As a control, the $E_h$ profile of the control experiment [simple mixture Fe@C + Fe$^{2+}$/PP$_3$] (Fig. 4c, dark red bars) demonstrates that this system is unable to create the appropriate reducing environment, substantiating its minimal reactivity in FA dehydrogenation.
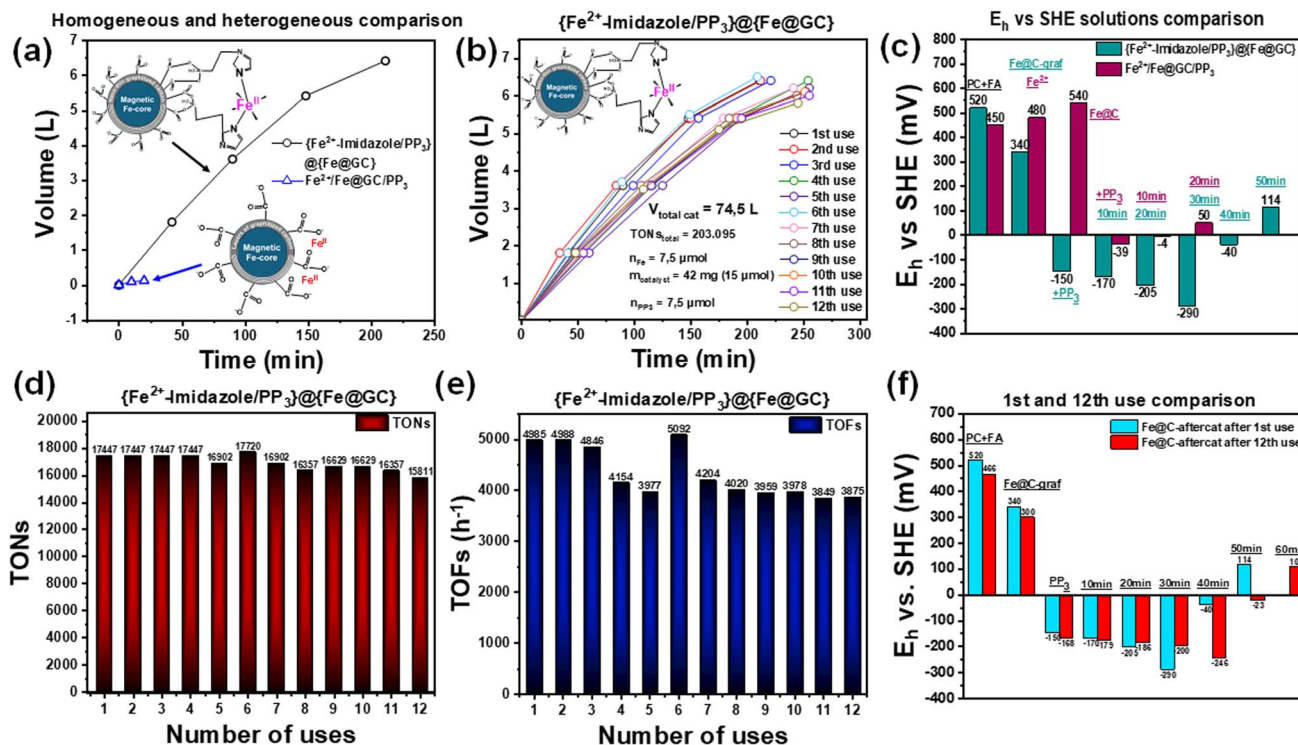
**21664** | *J. Mater. Chem. A*, 2025, **13**, 21659–21671

This journal is © The Royal Society of Chemistry 2025

Fig. 4 (a) Catalytic $H_2$–FADH by the {$Fe^{2+}$–imidazole/$PP_3$}@{Fe@GC} catalysts (black circles) or a simple mixture of Fe@GC + Fe/$PP_3$ (blue triangles). (b) Evaluation of catalyst {$Fe^{2+}$–imidazole/$PP_3$}@{Fe@GC} reusability: gas production over time for up to 12 reuses. (c) Solution potential mapping ($E_h$ vs. SHE) for {$Fe^{2+}$–imidazole/$PP_3$}@{Fe@GC} (green bars) or simple mixture of Fe@GC + Fe/$PP_3$ (purple bars). (d) Turnover numbers (TONs) recorded across multiple catalytic cycles. (e) Turnover frequencies (TOFs) observed for each catalytic cycle. (f) Comparative $E_h$ profile between the 1st and 12th catalytic use.

Table 2 Overall FADH catalytic data over 12th consecutive uses for the {$Fe^{2+}$–imidazole}@{Fe@GC} material

| Fe@C-graf material | Mass (mg) | Reaction time (min) | $VH_2 + CO_2$ (L) | Rate (ml $L^{-1}$) | TONs | TOFs ($h^{-1}$) | $V_{FA}$ (ml) |
|---|---|---|---|---|---|---|---|
| 1st use | 42 | 211 | 6.4 | 43 | 17 447 | 4985 | 8 |
| 2nd use | 42 | 212 | 6.4 | 43 | 17 447 | 4988 | 8 |
| 3rd use | 42 | 221 | 6.4 | 40 | 17 447 | 4846 | 8 |
| 4th use | 40 | 254 | 6.4 | 36 | 17 447 | 4154 | 8 |
| 5th use | 40 | 255 | 6.2 | 35 | 16 902 | 3977 | 8 |
| 6th use | 39 | 209 | 6.5 | 44 | 17 720 | 5092 | 8 |
| 7th use | 38 | 241 | 6.2 | 36 | 16 902 | 4204 | 8 |
| 8th use | 38 | 244 | 6 | 38 | 16 357 | 4020 | 8 |
| 9th use | 35 | 252 | 6.1 | 36 | 16 629 | 3959 | 8 |
| 10th use | 35 | 251 | 6.1 | 36 | 16 629 | 3978 | 8 |
| 11th use | 34 | 255 | 6 | 35 | 16 357 | 3849 | 8 |
| 12th use | 34 | 245 | 5.8 | 38 | 15 811 | 3875 | 8 |
| Total | — | 2850 | 74,5 | — | 203 095 | — | 96 |

Overall, the present data demonstrate that [i] the {$Fe^{2+}$–imidazole/$PP_3$}@{Fe@GC} hybrid is highly efficient in $H_2$ production *via* FADH at near ambient conditions; [ii] the key parameter of the mechanism is the successful generation of reducing equivalent, hydrides, in accordance with the established mechanism of the [Fe-imid/$PP_3$]catalyst. This proves that the grafted {Fe-imid} retains all its catalytic functionalities while the {Fe@GC} particle acts as a support that promotes the $H_2$-FADH process.

### 3.2.1 Recollection–recyclability of the magnetic catalyst.
Here, we exploit the magnetic {Fe@GC} core as a means to easily recollect and reuse the {Fe@Carbon@Imidazole–$Fe^{2+}$/$PP_3$} catalyst. Thus, after the initial use, the catalyst was magnetically separated, washed with methanol, dried, and re-used in a fresh mixture of [solvent + FA + $PP_3$], *i.e.*, as in the first cycle. Under these conditions, the reaction successfully restarted up to 12 times; see Fig. 4b. The data, also shown in Table 2, demonstrate a stable $H_2$ production performance with minor variations. In

This journal is © The Royal Society of Chemistry 2025

*J. Mater. Chem. A*, 2025, **13**, 21659–21671 | **21665**

this way, the cumulative gas production over 12 cycles totaled 74.5 L ($H_2 + CO_2$), corresponding to 37.25 L of pure $H_2$ and an overall TON of 203 095, with a total FA consumption of 96 mL. The TONs and TOFs achieved per cycle are shown in Fig. 4d and e, respectively. Additionally, $E_h$ vs. SHE measurements for the 1st and 12th cycles revealed consistent electrochemical behavior (Fig. 4f), confirming that the catalyst did not undergo significant degradation or deactivation over repeated uses.

# 4. Discussion

The present data demonstrate [i] the {$Fe^{2+}$–imidazole/PP$_3$}@ {Fe@GC} is a promising catalyst for efficient $H_2$ production via FA dehydrogenation; [ii] the nanostructure ensures high recyclability, durability under repeated use, and significant FA-volume handling highlight its robustness under harsh conditions without performance deterioration; [iii] the magnetic-core allows easy recollection/reuse of the catalyst. These advantages provide a competitive edge compared to similar literature-reported catalytic systems,[26,75–78] further reinforcing its potential for practical applications in sustainable hydrogen production.

Hereafter, we have peered into the effect of prolonged re-use, specifically 12 times, on the physicochemical characteristics of the catalyst. The working hypothesis was that, in a robust system such as the present one, subtle changes that might otherwise be negligible become more discernible after 12 reuses.

## 4.1 Post catalytic characterization of {$Fe^{2+}$–imidazole/PP$_3$}@ {Fe@GC} material after prolonged use

Elemental analysis (Table S4 in ESI†) indicates that after 12 reuses, the atomic concentrations of iron and imidazole remained unchanged, suggesting the integrity of their grafting despite multiple catalytic cycles. Additionally, the detection of P atoms indicates PP$_3$ adsorption during catalysis. TEM-EDS analysis (Fig. S6d in the ESI†) also confirmed the presence of iron, oxygen, and carbon, and phosphorus, further supporting the adsorption of PP$_3$ onto the catalyst surface during catalytic operation. As shown in the TEM image (Fig. 2e), after 12 reuses, the core–shell structure remains intact, and the core with

$d = 0.198$ nm represents the α-Fe (1 1 0) phase. XRD data suggest progressive oxidation of $Fe_3O_4$, leading to the formation of maghemite ($Fe_2O_3$), while iron carbides ($Fe_5C_2$ and $Fe_3C$) remain structurally preserved (Fig. 2a). Additionally, the emergence of graftonite ($Fe_3(PO_4)_2$) was observed, which is likely attributed to the adsorption of the PP$_3$ additive, as corroborated by EDS. The observed shifts in the $2\theta$ values suggest modifications in the electronic structure of the material, aligning with trends identified in FT-IR data,[79,80] as shown hereafter.

FT-IR spectroscopy (Fig. 5b) revealed a broad absorption band at 3438 cm$^{-1}$, attributed to O–H and N–H stretching vibrations.[66] Additionally, characteristic peaks at 3043 cm$^{-1}$, 2933 cm$^{-1}$, 1427 cm$^{-1}$, and 1340 cm$^{-1}$ corresponded to aliphatic C–H stretching vibrations.[67] A distinct peak at 1791 cm$^{-1}$, assigned to C=O stretching,[81] was detected exclusively in the post-catalysis samples (Fe@C-aftercat), indicating residual formic acid (HCOOH) despite their extensive washing. The 1579 cm$^{-1}$ band was attributed to C=C aromatic vibrations, with an additional N–H stretching mode overlapping in the same region.[82] Of particular significance were the peaks at 1200 cm$^{-1}$ and 1054 cm$^{-1}$, which confirmed the presence of phosphine post-catalysis, corresponding to P=O and P–Ph vibrations, respectively. Furthermore, a peak at 700 cm$^{-1}$ was assigned to P–C stretching, derived most probably from PP$_3$ adsorbed on the catalyst surface. The peak at 1054 cm$^{-1}$ in the as-prepared catalyst spectrum was also associated with Si–O stretching, indicating the presence of Si-centres derived from the silane precursor used for [$Fe^{2+}$–imidazole] grafting.[83–85] Subtle shifts in FT-IR peaks of the post-catalysis samples, compared to those of PP$_3$, suggest modifications in bond strength and electron density, likely due to interactions involving grafted [$Fe^{2+}$–imidazole] and PP$_3$.[86,87] To further confirm PP$_3$ adsorption on the hybrid catalyst after 12 repetitive cycles, thermogravimetric analysis (TGA) was conducted on the residual solid. As illustrated in Fig. S1 in ESI,† organic mass loss increased from 14% for the unused catalyst (Fig. S1a†) to 34% (Fig. S1c†) for the after-catalysis sample in the temperature range of 200–550 °C, which is attributed to the decomposition of PP$_3$.

Following catalytic recycling, the Raman spectrum of the post-catalysis material showed that the intensity of the $I_D/I_G$
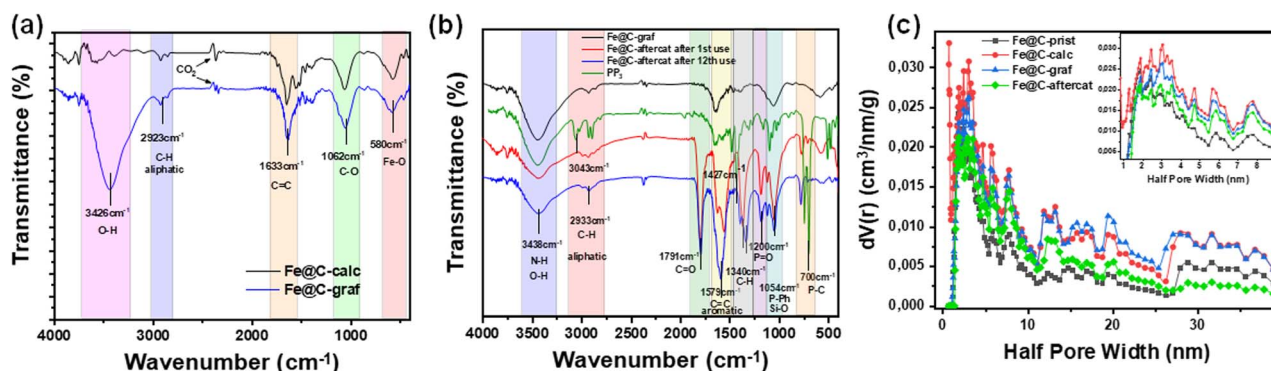


Fig. 5 FT-IR spectra of (a) a comparison of Fe@C-calc and Fe@C-graf and (b) comparison among Fe@C-graf, Fe@C-aftercat (1st use and 12th use), and PP$_3$. (c) Pore size distribution of all the hybrid materials using the DFT method.

**21666** | J. Mater. Chem. A, 2025, **13**, 21659–21671

This journal is © The Royal Society of Chemistry 2025

ratio decreased from 4.0 for the unused catalyst to 3.8, indicating an enhancement in crystallinity and a reduction in structural defects (see Fig. 3d). These findings are in agreement with our previous work, where a carbon matrix was restructured after FADH catalysis, decreasing its $I_D/I_G$ ratio.[42] Finally, BET analysis revealed a reduction in pore volume, with the specific surface area decreasing to 83 m$^2$ g$^{-1}$ for the recycled catalyst. This decrease is likely due to the adsorption of PP$_3$ on the carbon surface during the catalytic process, as evidenced by spectroscopies and TGA data.

In summary, the post-catalytic characterization confirms that the structural integrity of the graphitized core–shell catalyst remains largely preserved. A minor oxidation of the matrix occurred, i.e., by the acid HCOOH; however, its magnetic properties remain intact. The elemental profiles of iron and imidazole exhibit negligible variation after catalysis, underscoring the robustness and effectiveness of the catalyst despite the adsorption of PP$_3$. The catalyst maintained the integrity of both the graphitized core–shell carbon structure and the iron molecular catalytic centre while successfully operating in 12 cycles of FADH catalysis, demonstrating its multifunctional capability.

## 5. Conclusions

In this study, a novel magnetic graphitized core–shell catalyst, {Fe@Graphitized Carbon}@{Fe$^{2+}$–Imidazole}, was successfully designed and synthesized using the FSP process and chemical grafting. Diligent control of anoxic FSP enabled the formation of ultrafine graphitized carbon around the magnetic Fe core. The active metal catalytic center, comprising Fe$^{2+}$–imidazole, was grafted onto the particles via a straightforward synthesis approach utilizing a silane intermediate.

The so-synthesized {Fe@Graphitized Carbon}@{Fe$^{2+}$–Imidazole} catalyst exhibited remarkable durability and recyclability in H$_2$ production via HCOOH, achieving TONs of 203 095 while consuming 96 mL of formic acid over 12 catalytic cycles. A detailed analysis using TEM, Raman, XRD, and FTIR verified that the catalyst retained its nano-thin graphitized carbon shell structure and magnetic properties throughout the process up to the 12th reuse.

Technology-wise, the present work demonstrates that flame spray pyrolysis (FSP) is a promising, scalable technology that may pave the way towards the – long-envisaged – transition to industrial production of versatile nanocatalytic materials for H$_2$ production via formic acid (HCOOH) dehydrogenation.

## Data availability

The data supporting this study are not publicly available owing to commercial sensitivity, confidentiality restrictions and privacy concerns.

## Author contributions

C. G. catalytic experiments, methodology, investigation, data analysis, writing–original draft, and writing–review & editing; C.

D. materials synthesis via FSP, methodology, investigation, data analysis, writing–original draft, and writing–review & editing; S. S. TEM measurements; Y. D. conceptualization, data analysis, and writing–review & editing; M. L. conceptualization, data analysis, supervision, and writing–review & editing.

## Conflicts of interest

There are no conflicts to declare.

## Acknowledgements

## Notes and references

1 K. Mazloomi and C. Gomes, Hydrogen as an Energy Carrier: Prospects and Challenges, Renewable Sustainable Energy Rev., 2012, 16(5), 3024–3033, DOI: 10.1016/j.rser.2012.02.028.

2 N. Armaroli and V. Balzani, The Hydrogen Issue, ChemSusChem, 2011, 4(1), 21–36, DOI: 10.1002/cssc.201000182.

3 C. Guan, Y. Pan, T. Zhang, M. J. Ajitha and K. Huang, An Update on Formic Acid Dehydrogenation by Homogeneous Catalysis, Chem.–Asian J., 2020, 15(7), 937–946, DOI: 10.1002/asia.201901676.

4 S. Niaz, T. Manzoor and A. H. Pandith, Hydrogen Storage: Materials, Methods and Perspectives, Renewable Sustainable Energy Rev., 2015, 50, 457–469, DOI: 10.1016/j.rser.2015.05.011.

5 M. R. Usman, Hydrogen Storage Methods: Review and Current Status, Renewable Sustainable Energy Rev., 2022, 167, 112743, DOI: 10.1016/j.rser.2022.112743.

6 P. M. Modisha, C. N. M. Ouma, R. Garidzirai, P. Wasserscheid and D. Bessarabov, The Prospect of Hydrogen Storage Using Liquid Organic Hydrogen Carriers, Energy Fuels, 2019, 33(4), 2778–2796, DOI: 10.1021/acs.energyfuels.9b00296.

7 M. Grasemann and G. Laurenczy, Formic Acid as a Hydrogen Source – Recent Developments and Future Trends, Energy Environ. Sci., 2012, 5(8), 8171, DOI: 10.1039/c2ee21928j.

8 J. Eppinger and K.-W. Huang, Formic Acid as a Hydrogen Energy Carrier, ACS Energy Lett., 2017, 2(1), 188–195, DOI: 10.1021/acsenergylett.6b00574.

9 Z. Wang, S. Lu, J. Li, J. Wang and C. Li, Unprecedentedly High Formic Acid Dehydrogenation Activity on an Iridium Complex with an N , N ′-Diimine Ligand in Water, Chem.–Eur. J., 2015, 21(36), 12592–12595, DOI: 10.1002/chem.201502086.

10 D. A. Bulushev, M. Zacharska, A. S. Lisitsyn, O. Yu. Podyacheva, F. S. Hage, Q. M. Ramasse, U. Bangert and L. G. Bulusheva, Single Atoms of Pt-Group Metals Stabilized by N-Doped Carbon Nanofibers for Efficient

This journal is © The Royal Society of Chemistry 2025

J. Mater. Chem. A, 2025, 13, 21659–21671 | 21667

Hydrogen Production from Formic Acid, *ACS Catal.*, 2016, **6**(6), 3442–3451, DOI: **10.1021/acscatal.6b00476**.

11 S. Patra, H. Deka and S. K. Singh, Bis-Imidazole Methane Ligated Ruthenium(II) Complexes: Synthesis, Characterization, and Catalytic Activity for Hydrogen Production from Formic Acid in Water, *Inorg. Chem.*, 2021, **60**(18), 14275–14285, DOI: **10.1021/acs.inorgchem.1c01784**.

12 M. Solakidou, A. Gemenetzi, G. Koutsikou, M. Theodorakopoulos, Y. Deligiannakis and M. Louloudi, Cost Efficiency Analysis of H2 Production from Formic Acid by Molecular Catalysts, *Energies*, 2023, **16**(4), 1723, DOI: **10.3390/en16041723**.

13 S. Ge, J. Liu, L. Gong, X. Mo, C. Liu, X. Yi and P. He, Dehydrogenation of Aqueous Formic Acid by Iridium and Ruthenium Complexes with Nitrogen-rich Diamino-bis(1 *H* -1,2,4-triazole), *Eur. J. Inorg. Chem.*, 2024, **27**(2), e202300509, DOI: **10.1002/ejic.202300509**.

14 M. K. Rong, F. Holtrop, J. C. Slootweg and K. Lammertsma, Enlightening Developments in 1,3-P,N-Ligand-Stabilized Multinuclear Complexes: A Shift from Catalysis to Photoluminescence, *Coord. Chem. Rev.*, 2019, **382**, 57–68, DOI: **10.1016/j.ccr.2018.11.012**.

15 P. Knörr, N. Lentz and M. Albrecht, Efficient Additive-Free Formic Acid Dehydrogenation with a NNN–Ruthenium Complex, *Catal. Sci. Technol.*, 2023, **13**(19), 5625–5631, DOI: **10.1039/D3CY00512G**.

16 A. Boddien, B. Loges, F. Gärtner, C. Torborg, K. Fumino, H. Junge, R. Ludwig and M. Beller, Iron-Catalyzed Hydrogen Production from Formic Acid, *J. Am. Chem. Soc.*, 2010, **132**(26), 8924–8934, DOI: **10.1021/ja100925n**.

17 C.-P. Tsai, C.-Y. Chen, Y.-L. Lin, J.-C. Lan and M.-L. Tsai, Catalytic Dehydrogenation of Formic Acid Promoted by Triphos-Co Complexes: Two Competing Pathways for H$_2$ Production, *Inorg. Chem.*, 2024, **63**(4), 1759–1773, DOI: **10.1021/acs.inorgchem.3c02959**.

18 S. Enthaler, A. Brück, A. Kammer, H. Junge, E. Irran and S. Gülak, Exploring the Reactivity of Nickel Pincer Complexes in the Decomposition of Formic Acid to CO$_2$/H$_2$ and the Hydrogenation of NaHCO$_3$ to HCOONa, *ChemCatChem*, 2015, **7**(1), 65–69, DOI: **10.1002/cctc.201402716**.

19 M. Solakidou, M. Theodorakopoulos, Y. Deligiannakis and M. Louloudi, Double-Ligand Fe, Ru Catalysts: A Novel Route for Enhanced H2 Production from Formic Acid, *Int. J. Hydrogen Energy*, 2020, **45**(35), 17367–17377, DOI: **10.1016/j.ijhydene.2020.04.215**.

20 Y. Manaka, Y. Himeda, H. Matsumoto and T. Nanba, Immobilization and Characterization of SiO$_2$-Supported Ir-Complex Catalyst for Practical Hydrogen Generation from Formic Acid, *J. Jpn. Pet. Inst.*, 2017, **60**(4), 194–201, DOI: **10.1627/jpi.60.194**.

21 M. Yao, W. Liang, H. Chen and X. Zhang, Efficient Hydrogen Production from Formic Acid Using Nitrogen-Doped Activated Carbon Supported Pd, *Catal. Lett.*, 2020, **150**(8), 2377–2384, DOI: **10.1007/s10562-020-03141-y**.

22 T.-Y. Ding, Z.-G. Zhao, M.-F. Ran and Y.-Y. Yang, Superior Activity of Pd Nanoparticles Confined in Carbon Nanotubes for Hydrogen Production from Formic Acid Decomposition at Ambient Temperature, *J. Colloid Interface Sci.*, 2019, **538**, 474–480, DOI: **10.1016/j.jcis.2018.12.017**.

23 C. Ma, J. Duan, Y. Fu and J. Chang, Hydrogen Production from Additive-Free Formic Acid over Highly Active Metal Organic Frameworks-Supported Palladium-Based Catalysts, *Int. J. Hydrogen Energy*, 2021, **46**(7), 5259–5269, DOI: **10.1016/j.ijhydene.2020.11.058**.

24 P. S. Shinde, P. S. Suryawanshi, K. K. Patil, V. M. Belekar, S. A. Sankpal, S. D. Delekar and S. A. Jadhav, A Brief Overview of Recent Progress in Porous Silica as Catalyst Supports, *J. Compos. Sci.*, 2021, **5**(3), 75, DOI: **10.3390/jcs5030075**.

25 N. M. Julkapli and S. Bagheri, Graphene Supported Heterogeneous Catalysts: An Overview, *Int. J. Hydrogen Energy*, 2015, **40**(2), 948–979, DOI: **10.1016/j.ijhydene.2014.10.129**.

26 C. Gkatziouras, M. Solakidou and M. Louloudi, Efficient [Fe-Imidazole@SiO2] Nanohybrids for Catalytic H2 Production from Formic Acid, *Nanomaterials*, 2023, **13**(10), 1670, DOI: **10.3390/nano13101670**.

27 H. Jüntgen, Activated Carbon as Catalyst Support, *Fuel*, 1986, **65**(10), 1436–1446, DOI: **10.1016/0016-2361(86)90120-1**.

28 E. Lam and J. H. T. Luong, Carbon Materials as Catalyst Supports and Catalysts in the Transformation of Biomass to Fuels and Chemicals, *ACS Catal.*, 2014, **4**(10), 3393–3410, DOI: **10.1021/cs5008393**.

29 P. Serp and J. L. Figueiredo *Carbon Materials for Catalysis*; J. Wiley: Hoboken (N.J.), 2009.

30 E. Auer, A. Freund, J. Pietsch and T. Tacke, Carbons as Supports for Industrial Precious Metal Catalysts, *Appl. Catal., A*, 1998, **173**(2), 259–271, DOI: **10.1016/S0926-860X(98)00184-7**.

31 Z. Li and Q. Xu, Metal-Nanoparticle-Catalyzed Hydrogen Generation from Formic Acid, *Acc. Chem. Res.*, 2017, **50**(6), 1449–1458, DOI: **10.1021/acs.accounts.7b00132**.

32 S. Bai, A. Jia, J. Song, S. Cao, N. Wang and X. Liu, Metal-Support Interactions in Heterogeneous Catalytic Hydrogen Production of Formic Acid, *Chem. Eng. J.*, 2023, **474**, 145612, DOI: **10.1016/j.cej.2023.145612**.

33 M. A. Fraga, E. Jordão, M. J. Mendes, M. M. A. Freitas, J. L. Faria and J. L. Figueiredo, Properties of Carbon-Supported Platinum Catalysts: Role of Carbon Surface Sites, *J. Catal.*, 2002, **209**(2), 355–364, DOI: **10.1006/jcat.2002.3637**.

34 R. Eivazzadeh-Keihan, Z. Sadat, F. Lalebeigi, N. Naderi, L. Panahi, F. Ganjali, S. Mahdian, Z. Saadatidizaji, M. Mahdavi, E. Chidar, E. Soleimani, A. Ghaee, A. Maleki and I. Zare, Effects of Mechanical Properties of Carbon-Based Nanocomposites on Scaffolds for Tissue Engineering Applications: A Comprehensive Review, *Nanoscale Adv.*, 2024, **6**(2), 337–366, DOI: **10.1039/D3NA00554B**.

35 S. Zhang, B. Jiang, K. Jiang and W.-B. Cai, Surfactant-Free Synthesis of Carbon-Supported Palladium Nanoparticles and Size-Dependent Hydrogen Production from Formic

**21668** | *J. Mater. Chem. A*, 2025, **13**, 21659–21671

This journal is © The Royal Society of Chemistry 2025

Acid–Formate Solution, *ACS Appl. Mater. Interfaces*, 2017, **9**(29), 24678–24687, DOI: **10.1021/acsami.7b08441**.

36 F. Sanchez, M. H. Alotaibi, D. Motta, C. E. Chan-Thaw, A. Rakotomahevitra, T. Tabanelli, A. Roldan, C. Hammond, Q. He, T. Davies, A. Villa and N. Dimitratos, Hydrogen Production from Formic Acid Decomposition in the Liquid Phase Using Pd Nanoparticles Supported on CNFs with Different Surface Properties, *Sustainable Energy Fuels*, 2018, **2**(12), 2705–2716, DOI: **10.1039/C8SE00338F**.

37 M. Zacharska, L. G. Bulusheva, A. S. Lisitsyn, S. Beloshapkin, Y. Guo, A. L. Chuvilin, E. V. Shlyakhova, O. Y. Podyacheva, J. J. Leahy, A. V. Okotrub and D. A. Bulushev, Factors Influencing the Performance of Pd/C Catalysts in the Green Production of Hydrogen from Formic Acid, *ChemSusChem*, 2017, **10**(4), 720–730, DOI: **10.1002/cssc.201601637**.

38 S. Hafeez, S. M. Al-Salem, A. Bansode, A. Villa, N. Dimitratos, G. Manos and A. Constantinou, Computational Investigation of Microreactor Configurations for Hydrogen Production from Formic Acid Decomposition Using a Pd/C Catalyst, *Ind. Eng. Chem. Res.*, 2022, **61**(4), 1655–1665, DOI: **10.1021/acs.iecr.1c04128**.

39 M. Navlani-García, K. Mori, D. Salinas-Torres, Y. Kuwahara and H. Yamashita, New Approaches Toward the Hydrogen Production From Formic Acid Dehydrogenation Over Pd-Based Heterogeneous Catalysts, *Front. Mater.*, 2019, **6**, 44, DOI: **10.3389/fmats.2019.00044**.

40 E. N. Voskresenskaya, V. M. Kirilets, O. P. Taran and B. N. Kuznetsov, Hydrogen Production by the Heterogeneous Catalytic Dehydrogenation of Formic Acid: A Review, *Catal. Ind.*, 2024, **16**(3), 339–349, DOI: **10.1134/S2070050424700181**.

41 M. Yao, Y. Ye, H. Chen and X. Zhang, Porous Carbon Supported Pd as Catalysts for Boosting Formic Acid Dehydrogenation, *Int. J. Hydrogen Energy*, 2020, **45**(35), 17398–17409, DOI: **10.1016/j.ijhydene.2020.04.206**.

42 C. Gkatziouras, M. Solakidou and M. Louloudi, Formic Acid Dehydrogenation over a Recyclable and Self-Reconstructing Fe/Activated Carbon Catalyst, *Energy Fuels*, 2024, **38**(18), 17914–17926, DOI: **10.1021/acs.energyfuels.4c03191**.

43 Z. M. Sheng and J. N. Wang, Growth of Magnetic Carbon with a Nanoporous and Graphitic Structure, *Carbon*, 2009, **47**(14), 3271–3279, DOI: **10.1016/j.carbon.2009.07.043**.

44 E. P. Sajitha, V. Prasad, S. V. Subramanyam, S. Eto, K. Takai and T. Enoki, Synthesis and Characteristics of Iron Nanoparticles in a Carbon Matrix along with the Catalytic Graphitization of Amorphous Carbon, *Carbon*, 2004, **42**(14), 2815–2820, DOI: **10.1016/j.carbon.2004.06.027**.

45 R. Murthy and S. Chittor Neelakantan, Immobilization of Molecular Complexes on Graphitized Carbon Cloth as Stable and Hybrid Electrocatalysts for Enhanced Hydrogen Evolution Reaction and Oxygen Evolution Reaction, *Mater. Adv.*, 2022, **3**(22), 8201–8210, DOI: **10.1039/D2MA00764A**.

46 S. C. Tsang, V. Caps, I. Paraskevas, D. Chadwick and D. Thompsett, Magnetically Separable, Carbon-Supported Nanocatalysts for the Manufacture of Fine Chemicals, *Angew. Chem.*, 2004, **116**(42), 5763–5767, DOI: **10.1002/ange.200460552**.

47 R. Strobel and S. E. Pratsinis, Direct Synthesis of Maghemite, Magnetite and Wustite Nanoparticles by Flame Spray Pyrolysis, *Adv. Powder Technol.*, 2009, **20**(2), 190–194, DOI: **10.1016/j.apt.2008.08.002**.

48 W. Y. Teoh, R. Amal and L. Mädler, Flame Spray Pyrolysis: An Enabling Technology for Nanoparticles Design and Fabrication, *Nanoscale*, 2010, **2**(8), 1324–1347, DOI: **10.1039/C0NR00017E**.

49 F. Meierhofer and U. Fritsching, Synthesis of Metal Oxide Nanoparticles in Flame Sprays: Review on Process Technology, Modeling, and Diagnostics, *Energy Fuels*, 2021, **35**(7), 5495–5537, DOI: **10.1021/acs.energyfuels.0c04054**.

50 C. Dimitriou, P. Psathas, M. Solakidou and Y. Deligiannakis, Advanced Flame Spray Pyrolysis (FSP) Technologies for Engineering Multifunctional Nanostructures and Nanodevices, *Nanomaterials*, 2023, **13**(23), 3006, DOI: **10.3390/nano13233006**.

51 R. N. Grass; W. J. Stark and E.-K. Athanassiou Reducing Flame Spray Pyrolysis Method for the Production of Metal, Non-Oxidic, Ceramic and Reduced Metal Oxide Powders and Nano-Powders. *EP1760043A1*, March 7, 2007. **https://patents.google.com/patent/EP1760043A1/en**.

52 Y. Deligiannakis, A. Mantzanis, A. Zindrou, S. Smykala and M. Solakidou, Control of Monomeric Vo's *versus* Vo Clusters in $ZrO_{2-x}$ for Solar-Light H2 Production from H2O at High-Yield (Millimoles Gr−1 H−1), *Sci. Rep.*, 2022, **12**(1), 15132, DOI: **10.1038/s41598-022-19382-3**.

53 M. Solakidou, Y. Deligiannakis and M. Louloudi, Heterogeneous Amino-Functionalized Particles Boost Hydrogen Production from Formic Acid by a Ruthenium Complex, *Int. J. Hydrogen Energy*, 2018, **43**(46), 21386–21397, DOI: **10.1016/j.ijhydene.2018.09.198**.

54 Y. Ku, K. Xu, L. Yan, K. Zhang, D. Song, X. Li, S. Li, S. Cheng and C. Shan, Revealing the Atomic Mechanism of Diamond–Iron Interfacial Reaction, *Carbon Energy*, 2024, **6**(3), e440, DOI: **10.1002/cey2.440**.

55 H. Mao, J. Shu, Y. Fei, J. Hu and R. J. Hemley, The Wüstite Enigma, *Phys. Earth Planet. Inter.*, 1996, **96**(2), 135–145, DOI: **10.1016/0031-9201(96)03146-9**.

56 Y. Hadadian, H. Masoomi, A. Dinari, C. Ryu, S. Hwang, S. Kim, B. K. Cho, J. Y. Lee and J. Yoon, From Low to High Saturation Magnetization in Magnetite Nanoparticles: The Crucial Role of the Molar Ratios Between the Chemicals, *ACS Omega*, 2022, **7**(18), 15996–16012, DOI: **10.1021/acsomega.2c01136**.

57 Z. Li, L. Deng, I. A. Kinloch and R. J. Young, Raman Spectroscopy of Carbon Materials and Their Composites: Graphene, Nanotubes and Fibres, *Prog. Mater. Sci.*, 2023, **135**, 101089, DOI: **10.1016/j.pmatsci.2023.101089**.

58 A. Dychalska, P. Popielarski, W. Franków, K. Fabisiak, K. Paprocki and M. Szybowicz, Study of CVD Diamond Layers with Amorphous Carbon Admixture by Raman Scattering Spectroscopy, *Mater. Sci.-Pol.*, 2015, **33**(4), 799–805, DOI: **10.1515/msp-2015-0067**.

This journal is © The Royal Society of Chemistry 2025

*J. Mater. Chem. A*, 2025, **13**, 21659–21671 | **21669**

59 L. Bokobza, J.-L. Bruneel and M. Couzi, Raman Spectra of Carbon-Based Materials ite to Carbon Black) and of Some Silicone Composites, *C*, 2015, **1**(1), 77–94, DOI: **10.3390/c1010077**.

60 A. M. Martin and K. Righter, Melting of Clinopyroxene + Magnesite in Iron-Bearing Planetary Mantles and Implications for the Earth and Mars, *Contrib. Mineral. Petrol.*, 2013, **166**(4), 1067–1098, DOI: **10.1007/s00410-013-0910-5**.

61 D. L. A. De Faria, S. Venâncio Silva and M. T. De Oliveira, Raman Microspectroscopy of Some Iron Oxides and Oxyhydroxides, *J. Raman Spectrosc.*, 1997, **28**(11), 873–878, DOI: **10.1002/(SICI)1097-4555(199711)28:11<873::AID-JRS177>3.0.CO;2-B**.

62 Z. E. Brubaker, J. J. Langford, R. J. Kapsimalis and J. L. Niedziela, Quantitative Analysis of Raman Spectral Parameters for Carbon Fibers: Practical Considerations and Connection to Mechanical Properties, *J. Mater. Sci.*, 2021, **56**(27), 15087–15121, DOI: **10.1007/s10853-021-06225-1**.

63 N. Shimodaira and A. Masui, Raman Spectroscopic Investigations of Activated Carbon Materials, *J. Appl. Phys.*, 2002, **92**(2), 902–909, DOI: **10.1063/1.1487434**.

64 Y. Deligiannakis, E. Bletsa, E. Mouzourakis, M. Solakidou and K. Adamska, Carbon-Coated TiO2 Nanoparticles for Noble-Metal-Free Photocatalytic H2 Production from H2O, *ACS Appl. Nano Mater.*, 2024, **7**(10), 11621–11633, DOI: **10.1021/acsanm.4c01150**.

65 A. Ferrari, J. Robertson, P. Tan, S. Dimovski and Y. Gogotsi, Raman Scattering of Non–Planar Graphite: Arched Edges, Polyhedral Crystals, Whiskers and Cones, *Philos. Trans. R. Soc. London, Ser. A Philos. Trans.: Math., Phys. Eng. Sci.*, 2004, **362**(1824), 2289–2310, DOI: **10.1098/rsta.2004.1442**.

66 C.-W. Chang, N. Sekiya and K. Yoshihara, O-H Stretching Vibration in Fourier Transform Difference Infrared Spectra of Bacteriorhodopsin, *FEBS Lett.*, 1991, **287**(1–2), 157–159, DOI: **10.1016/0014-5793(91)80039-6**.

67 S.-M. Shin, J.-K. Park and S.-M. Jung, Changes of Aromatic CH and Aliphatic CH in In-Situ FT-IR Spectra of Bituminous Coals in the Thermoplastic Range, *ISIJ Int.*, 2015, **55**(8), 1591–1598, DOI: **10.2355/isijinternational.ISIJINT-2014-625**.

68 C. Dimitriou, L. Belles, N. Boukos and Y. Deligiannakis, {TiO₂/TiO₂ (B)} Quantum Dot Hybrids: A Comprehensible Route toward High-Performance [>0.1 Mol Gr$^{-1}$ h$^{-1}$] Photocatalytic H₂ Production from H₂O, *ACS Catal.*, 2024, **14**(23), 17919–17934, DOI: **10.1021/acscatal.4c05001**.

69 P. Stathi, M. Solakidou, M. Louloudi and Y. Deligiannakis, From Homogeneous to Heterogenized Molecular Catalysts for H2 Production by Formic Acid Dehydrogenation: Mechanistic Aspects, Role of Additives, and Co-Catalysts, *Energies*, 2020, **13**(3), 733, DOI: **10.3390/en13030733**.

70 M. Theodorakopoulos, Y. Deligiannakis and M. Louloudi, Solution-Potential and Solution-Hydrides as Key-Parameters in H2 Production via HCOOH-Dehydrogenation by Fe- and Ru-Molecular Catalysts, *Int. J. Hydrogen Energy*, 2024, **58**, 1608–1617, DOI: **10.1016/j.ijhydene.2024.01.317**.

71 M. Theodorakopoulos, M. Solakidou, Y. Deligiannakis and M. Louloudi, Double-Ligand [Fe/PNP/PP3] and Their Hybrids [Fe/SiO2@PNP/PP3] as Catalysts for H2-Production from HCOOH, *Energies*, 2024, **17**(16), 3934, DOI: **10.3390/en17163934**.

72 A. Gemenetzi, Y. Deligiannakis and M. Louloudi, Controlled Photoplasmonic Enhancement of H₂ Production via Formic Acid Dehydrogenation by a Molecular Fe Catalyst, *ACS Catal.*, 2023, **13**(14), 9905–9917, DOI: **10.1021/acscatal.3c01925**.

73 K. Gravvani, M. Solakidou and M. Louloudi, Highly-Efficient Reusable [Silica@Iminophosphine-Fe$^{II}$] Hybrids for Hydrogen Production via Formic Acid and Formaldehyde Dehydrogenation, *Chem.–Eur. J.*, 2025, **31**(16), e202404440, DOI: **10.1002/chem.202404440**.

74 A. Sotiriou, E. Aspri, Y. Deligiannakis and M. Louloudi, Engineering of Hybrid SiO2@{N-P-Fe} Catalysts with Double-Ligand for Efficient H2 Production from HCOOH, *Energies*, 2025, **18**(3), 514, DOI: **10.3390/en18030514**.

75 W. Gan, P. J. Dyson and G. Laurenczy, Hydrogen Storage and Delivery: Immobilization of a Highly Active Homogeneous Catalyst for the Decomposition of Formic Acid to Hydrogen and Carbon Dioxide, *React. Kinet. Catal. Lett.*, 2009, **98**(2), 205–213, DOI: **10.1007/s11144-009-0096-z**.

76 M. Navlani-García, K. Mori, Y. Kuwahara and H. Yamashita, Recent Strategies Targeting Efficient Hydrogen Production from Chemical Hydrogen Storage Materials over Carbon-Supported Catalysts, *NPG Asia Mater.*, 2018, **10**(4), 277–292, DOI: **10.1038/s41427-018-0025-6**.

77 F. Bertini, I. Mellone, A. Ienco, M. Peruzzini and L. Gonsalvi, Iron(II) Complexes of the Linear *Rac-* Tetraphos-1 Ligand as Efficient Homogeneous Catalysts for Sodium Bicarbonate Hydrogenation and Formic Acid Dehydrogenation, *ACS Catal.*, 2015, **5**(2), 1254–1265, DOI: **10.1021/cs501998t**.

78 A. Boddien, D. Mellmann, F. Gärtner, R. Jackstell, H. Junge, P. J. Dyson, G. Laurenczy, R. Ludwig and M. Beller, Efficient Dehydrogenation of Formic Acid Using an Iron Catalyst, *Science*, 2011, **333**(6050), 1733–1736, DOI: **10.1126/science.1206613**.

79 N. Pavithra and M. C. Robert, Tailoring Optical and Magnetic Properties in Mn2+-Substituted 2D Magnetic Semiconductor SnS2: A Powder XRD Approach for Electronic Structure Analysis, *J. Supercond. Novel Magn.*, 2025, **38**(1), 71, DOI: **10.1007/s10948-025-06908-9**.

80 V. Stanev, V. V. Vesselinov, A. G. Kusne, G. Antoszewski, I. Takeuchi and B. S. Alexandrov, Unsupervised Phase Mapping of X-Ray Diffraction Data by Nonnegative Matrix Factorization Integrated with Custom Clustering, *npj Comput. Mater.*, 2018, **4**(1), 43, DOI: **10.1038/s41524-018-0099-2**.

81 S. Ibrahim, A. Ahmad and N. Mohamed, Characterization of Novel Castor Oil-Based Polyurethane Polymer Electrolytes, *Polymers*, 2015, **7**(4), 747–759, DOI: **10.3390/polym7040747**.

82 Q. Ma, S. Dutta, K. C. -W. Wu and T. Kimura, Analytical Understanding of the Materials Design with Well-

21670 | *J. Mater. Chem. A*, 2025, **13**, 21659–21671

This journal is © The Royal Society of Chemistry 2025

Described Shrinkages on Multiscale, *Chem.–Eur. J.*, 2018, **24**(27), 6886–6904, DOI: 10.1002/chem.201704198.

83 N. Y. M. Isa, E. S. Sazali, R. Hisam, S. K. Ghoshal, S. K. M. Zain, N. H. Juma'in, S. N. S. Yaacob, Z. A. S. Mahraz, A. N. Harun, F. M. Noor, M. R. Sahar, K. A. Samah, M. S. Aziz, A. A. Salim and A. Awang, Physical, Structural, and Raman Spectroscopic Traits of Neodymium-Doped Lead Oxyfluoride Zinc Phosphate Glass, *J. Phys.:Conf. Ser.*, 2021, **1892**(1), 012027, DOI: 10.1088/1742-6596/1892/1/012027.

84 X. Yu and Q. Zhan Phosphate-Mineralization Microbe Repairs Heavy Metal Ions That Formed Nanomaterials in Soil and Water. In *Nanomaterials - Toxicity, Human Health and Environment*; ed. Clichici, S., Filip, A. and M. Do Nascimento, G., IntechOpen, 2020. doi: DOI: 10.5772/intechopen.84296.

85 E. Herth, R. Zeggari, J.-Y. Rauch, F. Remy-Martin and W. Boireau, Investigation of Amorphous SiOx Layer on Gold Surface for Surface Plasmon Resonance Measurements, *Microelectron. Eng.*, 2016, **163**, 43–48, DOI: 10.1016/j.mee.2016.04.014.

86 B. Rajamouli, R. Devi, A. Mohanty, V. Krishnan and S. Vaidyanathan, Effects of Electron-Withdrawing Groups in Imidazole-Phenanthroline Ligands and Their Influence on the Photophysical Properties of Eu[III] Complexes for White Light-Emitting Diodes, *New J. Chem.*, 2017, **41**(18), 9826–9839, DOI: 10.1039/C7NJ02291C.

87 Ş. Yurdakul and S. Badoğlu, Spectra, Vibrational Assignments, and Density Functional Calculations of Imidazo[1,2-a]Pyridine Molecule and Its Zn(II) Halide Complexes, *Struct. Chem.*, 2009, **20**(3), 423–434, DOI: 10.1007/s11224-009-9433-0.

This journal is © The Royal Society of Chemistry 2025

*J. Mater. Chem. A*, 2025, **13**, 21659–21671 | **21671**